EUROPEAN ORGANIZATION FOR NUCLEAR RESEARCH

CERN-EP/86-197
25 November 1986

MEASUREMENT OF STRONG-INTERACTION EFFECTS IN LIGHT ANTIPROTONIC ATOMS

H. Poth, H. Barth, G. Büche, A.D. Hancock*), H. Koch, Th. Köhler,
A. Kreissl**), U. Raich**), D. Rohmann and A. Wolf
Kernforschungszentrum Karlsruhe, Institut für Kernphysik, and Universität,
Institut für Experimentelle Kernphysik, Karlsruhe, Fed. Rep. Germany

L. Tauscher
Institute for Physics, University of Basle, Switzerland

A. Nilsson
Research Institute of Physics, Stockholm, Sweden

M. Suffert
Centre de Recherches Nucléaires, Strasburg, France

M. Chardalas and S. Dedoussis
Department of Nuclear Physics, University of Thessaloniki, Greece

H. Daniel, T. von Egidy, F.J. Hartmann, W. Kanert, H.S. Plendl***) and G. Schmidt
Physik Department der Technischen Universität, Munich, Fed. Rep. Germany

J.J. Reidy
Physics Department, University of Mississippi, University, Mississippi, USA

ABSTRACT

The strong-interaction effects in antiprotonic ^{6}Li, ^{7}Li, ^{14}N, ^{19}F, and ^{23}Na atoms were measured at the CERN antiproton facility, LEAR. For the 2p level we determined the shifts to be -215 ± 25 eV (^{6}Li) and -265 ± 20 eV (^{7}Li) and the widths to be 660 ± 170 eV (^{6}Li) and 690 ± 170 eV (^{7}Li). For the 3d level we obtained for the shifts -40 ± 30 eV (^{14}N), -440 ± 70 eV (^{19}F), and -2.1 ± 0.3 keV (^{23}Na), and for the widths 0.135 ± 0.016 (^{6}Li), 0.129 ± 0.013 eV (^{7}Li), 218 ± 75 eV (^{14}N), 1365 ± 150 eV (^{19}F), and 2.9 ± 1.1 keV (^{23}Na).

(Submitted to Nuclear Physics A)

---

*) Present address: EG&G, Los Alamos, New Mexico, USA
**) At present at CERN, Geneva, Switzerland
***) Permanent address: Physics Department, Florida State University, Tallahassee, Florida, USA

1. INTRODUCTION

The measurement of X-ray spectra of antiprotonic atoms is a well-established method for obtaining experimental information on the $\bar{p}$-nucleus force. With the high-intensity and pure antiproton beams of the Low-Energy Antiproton Ring (LEAR) at CERN these experiments are now reaching, for the first time, high precision within running times of only a few hours per target. This has to be compared with previous experiments, which accumulated data within beam times of several weeks.

The experiment was set up to exploit the new experimental possibilities at LEAR. The original experimental programme was outlined at the 2nd LEAR Workshop in Erice [1]. We have previously reported on preliminary results [2]. Final results concerning the measurement of isotope effects and the 4f level widths are now available [3,4]. Also a part of the data concerning the search for spin-orbit effects was published recently [5] as well as the E2 nuclear-resonance effect [6].

In the present work we report on further results of the systematic study of strong-interaction effects in light elements. We have measured the width of the 3d level for antiprotonic atoms with nuclear masses between A = 6 and A = 23. The shift of the 3d level could be extracted for atoms between A = 14 and A = 23. The object of this systematic study was to follow the evolution of strong-interaction effects with the mass A and the nuclear charge Z in one specific atomic level. These data are complemented with results from ^{6}Li and ^{7}Li containing also information on the shifts and widths of the atomic 2p level.

In section 2 we describe the experimental set-up and the data acquisition, and in section 3 the evaluation of the data. The results are presented in section 4 and compared with theoretical predictions in section 5.

2. EXPERIMENTAL SET-UP AND DATA ACQUISITION

The experiment was located in the M1 beam line of the LEAR experimental hall. The antiproton beam of about 300 MeV/c incident momentum was detected with a beam telescope consisting of two scintillation counters in coincidence and moderated in two wedge-shaped polyethylene blocks so as to stop in the 300 mg/cm^2 target (fig. 1). The range of the antiprotons was adjusted by setting the remotely controlled moderator to a thickness corresponding to the centre of the count rate plateau. The width of the range curve was of the order of 170 mg/cm^2 (essentially due to range straggling). The size of the $\bar{p}$ beam was measured before moderation and found to be 7 mm vertically and 9 mm horizontally (FWHM). Owing to multiple scattering during moderation it blew up to approximately 2.5 cm in diameter at the target which had a lateral extension of about 3 × 3 cm^2 in most cases. The relevant information about the targets and the number of stopped antiprotons are given in table 1.

The results for ^{14}N were obtained as a by-product from the $\bar{p}$-atomic X-ray spectra of ^{138}Ba [target $Ba(NO_3)_2$], as well as from the air contamination in the $\bar{p}$-atomic ^{6}Li, ^{7}Li, and ^{40}Ca X-ray spectra. (The results on $\bar{p}^{40}$Ca will be the subject of a future publication.) The target was surrounded by four to six solid-state [Si(Li), Ge, Ge(Li)] detectors placed at distances between 12 cm and 27 cm, depending on the size of the detector. For the low-energy spectrum of ^{6}Li and ^{7}Li the main information on the strong-interaction effects came from a 210 mm^2 × 10 mm Ge detector, with a resolution of 425 eV at 26 keV. For ^{14}N, ^{19}F, and ^{23}Na we obtained the data from two intrinsic Ge detectors [500 mm^2 × 13 mm and 200 mm^2 × 7 mm], each with a resolution of about 550 eV at 60 keV. We obtained additional information for ^{19}F from a 1900 mm^2 × 13 mm Ge detector with a resolution of 900 eV at 90 keV. The single rates of the detectors were between 10^2 and 10^4 s^{-1} depending on their size and their distance from the target.

The detector electronics consisted of a fast logical branch to establish a coincidence with the telescope trigger and a linear branch to measure the pulse height. The latter comprised a spectroscopy amplifier and a highly linear analog-to-digital converter (ADC) [13 bit]. Each fast branch contained a

timing filter amplifier (TFA) and two constant-fraction discriminators (CFD) for a lower and upper thresholds. The coincidence window with the telescope trigger was 100 ns wide; however, the width of the timing curve, entirely due to the time resolution of the solid-state detectors, was minimized to 15 ns optimizing TFA and CFD. A time-to-digital converter (TDC) was started by the telescope trigger (in coincidence with the fast pulse of any solid-state detector) and stopped with an individual fast signal of at least one of the solid-state detectors. In addition, an individual pattern bit in a pattern unit was set for each detector which fired in coincidence with the telescope trigger. The trigger for the computer was given by a coincidence between the telescope and at least one of the X-ray detectors.

Anticipating high count rates for this experiment, a special data-acquisition system was developed [7] which consisted of a MC68000 microprocessor with 2.5 Mbyte memory and a PDP 11/34 computer. During a spill the microprocessor handled the readout of the experimental data. Pulse-height (ADC) and TDC information from each active detector were stored in a two-dimensional array. In the spill pause (15–20 min) the PDP accessed this memory, transferred the complete data to a magnetic tape, and projected the two-dimensional spectra on the energy and on the time axis. These projected energy and time spectra were written on the disk of the PDP. The microprocessor memory was thereafter cleared and thus again ready for new data taking. The whole transfer took three minutes. A home-built CAMAC unit (CAMPORT) [8] controlled the data flow between the experiment (ADC, TDC, pattern unit) and the microprocessor memory on the one hand, and between the PDP and the microprocessor on the other hand. This was done in such a way that only one of the two computers had access to the microprocessor memory (data) at a time. However, the PDP, with a separate CAMAC crate, controlled independently the various counters and moderator settings. Figure 2 shows a scheme of the data flow between the detector electronics, the microprocessor, and the PDP. Once on the disk of the PDP the data were checked and then transferred through the CERN-IBM (CERNET) to a second minicomputer [LSI 11/23], and to the CERN-CDC, and through the EARN-network to the KfK-IBM, for off-line evaluation.

A part of the two-dimensional spectrum of the X-rays from the ^{7}Li target is shown in the scatter plot of fig. 3 which also gives the projection on the energy and on the time axis. The projection on the energy axis for the antiprotonic X-ray spectra of the two lithium targets and of the sodium-fluoride target is displayed in more detail in fig. 4. As can be seen from the plots, the spectra contain an exceptionally low background and are nearly free from contamination lines. The only contamination came from the aluminium of the target frame and the target holder, and from the detector housings in which scattered antiprotons or annihilation pions stopped, in their turn forming exotic atoms. The large number of X-ray lines of known energy provided a very useful on-line energy calibration.

3. DATA EVALUATION

Most of the data evaluation was done on the LSI 11/23 computer with the program FIT [9] using the projection of the two-dimensional histograms on the energy axis without any time cuts. Energy calibration and energy resolution of each detector were determined from the pre- and post-run calibration spectra, obtained with radioactive sources. This calibration was further refined during the following evaluation procedure. First, the antiprotonic X-ray spectra were fitted spill by spill. The X-ray energies [10], converted into channel numbers according to the source calibration, were used initially. Each X-ray line was treated as one peak. Background lines were also fitted and identified with the help of the determined energy. From the X-ray lines not perturbed by strong interaction we deduced a preliminary on-line calibration for energy and resolution. On this basis the spectra were refitted, now treating every $\bar{p}$-atomic line as a fine structure (FS) triplet. The relative intensity ratios, the Gaussian widths, and the positions within each triplet were linked and varied as three free parameters instead of nine.

Since all studied nuclei have a non-zero nuclear spin (J^{π}) the atomic levels will have magnetic-dipole and electric-quadrupole hyperfine-structure (HFS) in addition to the fine-structure (FS) splitting. The calculated binding energies [10] of the last two observable levels are listed in table 2. Columns 4 and 8 indicate the FS level energies, columns 6 and 10 the ones for the HFS. The transition energies can be calculated from those. In order to estimate the influence of this HFS on the detected line shape we made a Monte Carlo simulation of the 4 → 3 transitions including HFS and assuming the relative intensities for the allowed transitions to be given by the appropriate Clebsch-Gordan coefficients. The widths of the individual lines were fixed according to the experimental resolution and a presumed Lorentzian width. In all cases but ^{23}Na we were able to fit the simulated complex with a FS triplet only, reproducing exactly the total intensities and Lorentzian widths given as input values for the Monte Carlo simulation. Therefore only FS triplets were considered in the analysis.

The final energy calibration was done with those antiprotonic X-ray lines which were not affected by strong-interaction effects. It turned out that the offset of the on-line energy calibration depended on the individual antiproton stop rate for each spill, the changes in the slope being negligible. A simple two-parameter calibration polynomial was sufficient. The $\bar{p}$-atomic X-ray lines influenced by strong interaction were fitted with a Lorentzian curve convoluted with a Gaussian curve using the complex error function [11]. The Lorentzian widths within a triplet were taken to be equal, the Gaussian widths were set according to the energy resolution, and the energy-distances of the FS components were taken from the pure electromagnetic energy differences neglecting the possibility of a spin-orbit term in the $\bar{p}$-nucleus interaction.

Apart from the relatively large HFS splitting, the evaluation of the 4 → 3 transition in ^{23}Na was difficult because of its very small yield and its large shift and width. After a careful check we assumed that the $\bar{p}^{19}$F 5 → 3 and $\bar{p}^{27}$Al 6 → 4 were the only background lines. A cascade fit to $\bar{p}^{19}$F intensities [4] indicated that the 5 → 3 intensity should be only 5‰ of that ot the 5 → 4. This intensity, corrected for efficiencies, and the strong-interaction effect values for ^{19}F from table 3 were fixed in the fitting of the ^{23}Na 4 → 3 region. For the $\bar{p}^{27}$Al 6 → 4 peak we presumed the (efficiency corrected) intensity of 10% of the $\bar{p}^{27}$Al 5 → 4 derived from spectra of targets (e.g. oxygen) where this line is not hidden by other lines.

4. RESULTS

The best fits for the last observable lines are shown in figs. 5 and 6. The results for the shifts and widths of the 2p level of ^{6}Li and ^{7}Li as well as for the 3d level of ^{14}N, ^{19}F, and ^{23}Na are shown in table 3. From the intensity ratios we also derived the widths Γ_{up} of the 3d level of ^{6} Li and ^{7}Li, in the same way as described in ref. [4]. These results are also given in table 3. In all cases the statistical errors are below 10%. Systematic errors introduced through the fitting were determined by varying the then-fixed background and the resolution within their statistical errors. The variations of the beam properties from spill to spill resulted in variations of shifts and widths which were much larger than the statistical errors and gave rise to the large systematic errors. These contributions to the systematic errors were obtained by fitting a Gaussian to the frequency distribution for each of the two quantities (ϵ, Γ_{low}). Owing to the limited running time at LEAR there was no opportunity to study these effects in detail. The systematic errors were added quadratically to the statistical ones and this gave the total error. The values given in table 3 are also plotted in fig. 7 for clarity.

5. DISCUSSION

The outcome of this experiment can be compared with previous measurements [12–15] and theoretical calculations [16–22], all summarized in table 4. Our new values for ^{6}Li and ^{7}Li agree well with our pre-LEAR results [13], although the 2p level widths are much larger now. All the results are

shown in the ϵ–Γ plot of fig. 8. Although our systematic errors are conservative our results for the lithium isotopes are a factor of 2 to 3 more precise than the previous measurements. Within this accuracy we do not observe an isotope effect in this isotope pair.

The only theoretical calculation for the lithium isotopes was done by Dumbrajs et al. [16]. They constructed an $\bar{p}$–nucleus potential from the $\bar{p}N$ K-matrices, corresponding to the central, spin-orbit and tensor parts of the Dover–Richard $N\bar{N}$ potential. They calculated the shifts and widths (note that they give $\Gamma/2$) for the $j = 3/2$ and $j = 1/2$ components of the 2p level in ^{6}Li and ^{7}Li by neglecting the spin-orbit and tensor parts. Their shift and width in the $j = 1/2$ state are about 30 eV larger than in the $j = 3/2$ state. The average values, given in table 4, do not differ for ^{6}Li and ^{7}Li. Their results are in fairly good agreement with our measurements.

For ^{14}N there are a number of calculations which all reproduce the experimental results (fig. 8) and thus we cannot judge the relative quality of the theoretical calculations. This is not surprising since in ^{14}N the strong-interaction effects are relatively small so that they cannot be measured with high relative accuracy. As a consequence, the measurement of the shift and width in ^{14}N alone is not a sensible test of potential models.

The strong-interaction shifts and widths in antiprotonic ^{19}F and ^{23}Na are measured for the first time. The observed strong-interaction effects are large. For these nuclei Sparrow [22] deduced the shifts and widths, given in table 4, from a relativistic approach to the $\bar{p}$–nucleus interaction. From the relativistic impulse approximation in conjunction with the Dirac equation the low-energy $\bar{p}$–nucleus potential was constructed. An isospin averaged amplitude was used and the neutron densities were taken equal to the proton densities. The shifts calculated by Sparrow [22] for the 3d level of ^{19}F and ^{23}Na are nearly two standard deviations lower than our measurement, while the width of the 3d level is barely in agreement with our value for ^{19}F, and disagrees with that in ^{23}Na. The feature of overestimating the width and underestimating the shift can be observed also for Sparrow's calculation [22] of the strong-interaction effects in ^{16}O in comparison with our data [3]. However, in a recent calculation [23] he found full agreement with our oxygen data.

With an improved black-sphere model Kaufmann and Pilkuhn [17] recalculated the level widths of antiprotonic atoms. Their values, given in table 4, agree with our values in all cases except ^{23}Na and the 3d width in the lithium isotopes.

Since the $\bar{p}$–nucleus interaction is very strong we expect it to take place well-localized at the surface of the nucleus. That means shift and width should depend mainly on the overlap of the Coulomb wave function with the nucleus. Under the simple assumption of a uniform nucleon distribution, the overlap scales as $\sim (ZA^{1/3})^{2\ell+3}$, where Z is the charge and A the mass of the nucleus, and $\ell = n - 1$ is the orbital angular momentum of the atomic level. This scaling behaviour is compared with the data in fig. 9, where we have plotted the strong-interaction effects in the 3d level divided by $(ZA^{1/3})^7$. While the shifts very closely obey this simple scaling law, the widths increase less rapidly with A than one would expect. Also shown in this plot are the theoretical calculations of Sparrow [22] and Kaufmann and Pilkuhn [17].

6. CONCLUSIONS

There are a number of new precise data on strong-interaction effects available now from measurements at LEAR. In earlier publications [3,4] and in this work we have presented data on strong-interaction effects in light antiprotonic atoms and compared them with existing theoretical calculations. Most of the recent calculations come close to the results of our measurements but none of them reproduces all of our data simultaneously. In the comparison of the data presented here with theoretical predictions, we observe that the model based on the relativistic impulse approximation comes close to our measured data, although it seems that this approach overestimates the widths and underestimates the shifts. For a more detailed check of this approach it would also be useful to have

the strong-interaction effects in ^{6}Li and ^{7}Li and the HFS computed. The phenomenological black-sphere model gives also a gross agreement with our data.

It would be desirable to apply the method of Dumbrajs et al. [16] to ^{19}F and ^{23}Na, since, within their approach, they are able to calculate the HFS, which we considered negligible in our analysis. However, at least in ^{19}F, where there are only a few HFS lines, we should be able to verify whether that is justified.

In order to perform a conclusive check of the various potential models, more theoretical calculations for the measured atoms are needed. In particular, it is important to study the dependence of the strong-interaction effects on nuclear-shape parameters.

Acknowlegdements

We would like to thank the LEAR staff for their helpful collaboration during the data taking. We are indebted to the design and construction departments of the Kernforschungszentrum Karlsruhe for their efforts in constructing the hardware of the experimental set-up. We are grateful to H. Hagn, J. Hauth, and P. Stoeckel for their technical assistance. The work was supported by the Bundesministerium für Forschung und Technologie of the Federal Republic of Germany, by the Deutsche Forschungsgemeinschaft, by the Swiss National Science Foundation, and by the US National Science Foundation.

REFERENCES

[1] H. Poth, Physics with antiprotonic atoms, Proc. 2nd LEAR Workshop on Physics with Low-Energy Cooled Antiprotons, Erice, 1982 (eds. U. Gastaldi and R. Klapisch) (Plenum, New York, 1984), p. 567.

[2] H. Koch et al., Antiprotonic atom spectroscopy at LEAR (PS176), Proc. 7th European Symposium on Antiproton Interaction, Durham, 1984 (Inst. Phys. Conf. Ser. No. 73: Adam Hilger, Bristol, 1985), p. 175;
H. Poth et al., Antiprotonic atoms, achievements and perspectives, Proc. 3rd LEAR Workshop on Physics with Antiprotons at LEAR in the ACOL era, Tignes, 1985 (eds. U. Gastaldi, R. Klapisch, J.M. Richard and J. Tran Thanh Van) (Éditions Frontières, Gif-sur-Yvette, 1986), p. 581.

[3] Th. Köhler et al., Phys. Lett. **176B** (1986) 327.

[4] D. Rohmann et al., Z. Phys. **A325** (1986) 261.

[5] A. Kreissl, Thesis, University of Karlsruhe, Kernforschungszentrum Karlsruhe, KfK 4128 (1986);
A. Kreissl et al., Measurement of the antiprotonic magnetic moment and a determination of the spin-orbit term for the antiproton-nucleus interaction, Proc. 8th European Symposium on Nucleon–Antinucleon Interactions, Thessaloniki, 1986, to be published.

[6] W. Kanert et al., Phys. Rev. Lett. **56** (1986) 2368.

[7] U. Raich, Thesis, University of Karlsruhe, Kernforschungszentrum Karlsruhe, KfK 3712 (1984).

[8] M. Meyer, S. Carius and P. Schmid, CAMPORT, CERN–EP Internal Report 83–02, Geneva (1983).

[9] D. Rohmann and Th. Köhler, Computer Code FIT, Kernforschungszentrum Karlsruhe, KfK 4184 (1986).

[10] E.F. Borie, Phys. Rev. **A28** (1983) 555;
B. Jödicke, Kernforschungszentrum Karlsruhe, KfK 3933 (1985).

[11] C.J. Batty, S.D. Hoath and B.L. Roberts, Nucl. Instrum. Methods **137** (1976) 179.

[12] P. Roberson et al., Phys. Rev. **C16** (1977) 1945.

[13] R. Guigas et al., Phys. Lett. **137B** (1984) 323.

[14] P. Barnes et al., Phys. Rev. Lett. **29** (1972) 1132.

[15] H. Poth et al., Nucl. Phys. **A294** (1978) 435.

[16] O. Dumbrajs et al., Nucl. Phys. **A457** (1986) 491.

[17] W.B. Kaufmann and H. Pilkuhn, Phys. Lett. **166B** (1986) 279;
W.B. Kaufmann, private communication.

[18] A. Deloff and J. Law, Phys. Rev. **C10** (1974) 2657, and Erratum, Phys. Rev. **C11** (1975) 1067.

[19] H. Nishimura and T. Fujita, Phys. Lett. **60B** (1976) 413.

[20] J.F. Haak, A. Lande and F. Iachello, Phys. Lett. **66B** (1977) 16.

[21] T. Suzuki and H. Narumi, Nucl. Phys. **A426** (1984) 413.

[22] D.A. Sparrow, Phys. Rev. **C33** (1986) 287.

[23] D.A. Sparrow, Spin and isospin effects in a relativistic treatment of $\bar{p}$-atom shifts and widths, Preprint Univ. Pennsylvania, Philadelphia, September 1986.

Table 1

Targets used for this experiment and the number of stopped antiprotons. The target thickness was 300 mg/cm^2 in all cases.

Nucleus	Target	10^6 stopped antiprotons	Spills[a)]
^{6}Li	^{6}Li	295	2
^{7}Li	^{7}Li	385	2
^{14}N	$Ba(NO_3)_2$ and/or air	1136	13
^{19}F	NaF	647	5
^{23}Na	NaF	647	5

a) Antiproton extraction periods of one hour

Table 2

Hyperfine-structure splitting of 2p, 3d, and 4f levels

Nucleus	J^{π}	Upper level				Lower level			
		n,l,j	[keV]	F	[keV]	n,l,j	[keV]	F	[keV]
^{6}Li	1^{+}	3,2,$^{5}/_{2}$	21.4335	$^{7}/_{2}$	21.4334	2,1,$^{3}/_{2}$	48.3083	$^{5}/_{2}$	48.3076
				$^{5}/_{2}$	21.4335			$^{3}/_{2}$	48.3076
				$^{3}/_{2}$	21.4338			$^{1}/_{2}$	48.3116
		3,2,$^{3}/_{2}$	21.4358	$^{5}/_{2}$	21.4358	2,1,$^{1}/_{2}$	48.3316	$^{3}/_{2}$	48.3313
				$^{3}/_{2}$	21.4358			$^{1}/_{2}$	48.3321
				$^{1}/_{2}$	21.4361				
^{7}Li	$^{3}/_{2}^{-}$	3,2,$^{5}/_{2}$	21.8822	4	21.8833	2,1,$^{3}/_{2}$	49.3207	3	49.3347
				3	21.8789			2	49.2676
				2	21.8820			1	49.3440
				1	21.8873			0	49.4185
		3,2,$^{3}/_{2}$	21.8847	3	21.8854	2,1,$^{1}/_{2}$	49.3449	2	49.3439
				2	21.8815			1	49.3467
				1	21.8862				
				0	21.8906				
^{14}N	1^{+}	4,3,$^{7}/_{2}$	71.5343	$^{9}/_{2}$	71.5331	3,2,$^{5}/_{2}$	127.3371	$^{7}/_{2}$	127.3302
				$^{7}/_{2}$	71.5374			$^{5}/_{2}$	127.3302
				$^{5}/_{2}$	71.5323			$^{3}/_{2}$	127.3568
		4,3,$^{5}/_{2}$	71.5513	$^{7}/_{2}$	71.5503	3,2,$^{3}/_{2}$	127.4181	$^{5}/_{2}$	127.4133
				$^{5}/_{2}$	71.5543			$^{3}/_{2}$	127.4354
				$^{3}/_{2}$	71.5490			$^{1}/_{2}$	127.3979
^{19}F	$^{1}/_{2}^{+}$	4,3,$^{7}/_{2}$	120.4425	4	120.4397	3,2,$^{5}/_{2}$	214.4028	3	214.3901
				3	120.4461			2	214.4205
		4,3,$^{5}/_{2}$	120.4906	3	120.4884	3,2,$^{3}/_{2}$	214.6309	2	214.6230
				2	120.4935			1	214.6441
^{23}Na	$^{3}/_{2}^{+}$	4,3,$^{7}/_{2}$	181.5906	5	181.5416	3,2,$^{5}/_{2}$	323.2372	4	322.9627
				4	181.6729			3	323.7922
				3	181.6254			2	323.3534
				2	181.5008			1	322.5557
		4,3,$^{5}/_{2}$	181.6998	4	181.6580	3,2,$^{3}/_{2}$	323.7525	3	323.5595
				3	181.7841			2	324.2904
				2	181.7178			1	323.5868
				1	181.5971			0	322.8778

Table 3

Experimental strong-interaction shifts and widths for the $\bar{p}$-atomic 2p and 3d levels. The first numbers in brackets give the statistical errors, the second numbers in brackets the total errors. [All energies in eV.]

Nucleus	$-\epsilon_{2p}$	Γ_{2p}	$-\epsilon_{3d}$	Γ_{3d}
^{6}Li	215 (17) (25)	660 (55) (170)		0.135 (0.016)
^{7}Li	265 (15) (20)	690 (50) (170)		0.129 (0.013)
^{14}N			40 (3) (30)	218 (13) (75)
^{19}F			440 (16) (70)	1365 (50) (150)
^{23}Na			2080 (160) (300)	2900 (640) (1100)

Table 4

Comparison of our results with other experiments and with theory. [All energies in eV.]

	^{6}Li			^{7}Li		
	$-\epsilon_{2p}$	Γ_{2p}	Γ_{3d}	$-\epsilon_{2p}$	Γ_{2p}	Γ_{3d}
Exp.:						
This	215 (25)	660 (170)	0.135 (0.016)	265 (20)	690 (170)	0.129 (0.013)
[12]	70 (170)	340 (310)	0.34 (1.45)	268 (81)	180 (140)	0.27 (0.18)
[13]	230 (72)	443 (210)	0.13 (0.05)	336 (60)	456 (190)	0.21 (0.06)
Theor.:						
[16]	205	536		203	569	
[17]		647	0.23		766	0.31

	^{14}N		^{19}F		^{23}Na	
	$-\epsilon_{3d}$	Γ_{3d}	$-\epsilon_{3d}$	Γ_{3d}	$-\epsilon_{3d}$	Γ_{3d}
Exp.:						
This	40 (30)	218 (75)	440 (70)	1365 (150)	2080 (300)	2900 (1100)
[14]	39 (51)	173 (34)				
[15]	3 (50)	205 (70)				
Theor.:						
[17]		154		1421		4933
[18]	31	157				
[19]	36	209				
[20]	51	141				
[21]	53	167				
[22]	20	204	302	1507	1475	5253

Figure captions

Fig. 1 Set-up of our experiment (PS176).

Fig. 2 Flow chart of the data-acquisition system.

Fig. 3 Energy–time scatter plot and projections on energy and time axis for the $3 \rightarrow 2$ region of $\bar{p}^7$Li.

Fig. 4 $\bar{p}$-atomic X-ray spectrum from the two lithium targets and from the sodium fluoride target.

Fig. 5 Fits to the $3 \rightarrow 2$ complex of antiprotonic ^{6}Li and ^{7}Li atoms.

Fig. 6 Fits to the $4 \rightarrow 3$ complex of antiprotonic ^{14}N, ^{19}F, and ^{23}Na atoms.

Fig. 7 Experimental strong-interaction shifts and widths as a function of the atomic weight A.

Fig. 8 Experimental and theoretical strong-interaction shifts and widths for the two lithium isotopes and for the nitrogen in ϵ–Γ plots.

Fig. 9 Strong-interaction shifts and widths of the $\bar{p}$-atomic 3d level, scaled according to the overlap of the antiproton with the nucleus as described in the text. ■, ●: shifts, widths from this experiment. ⊞, ⊕: shifts, widths from ref. [22]. ⊗: widths from ref. [17].

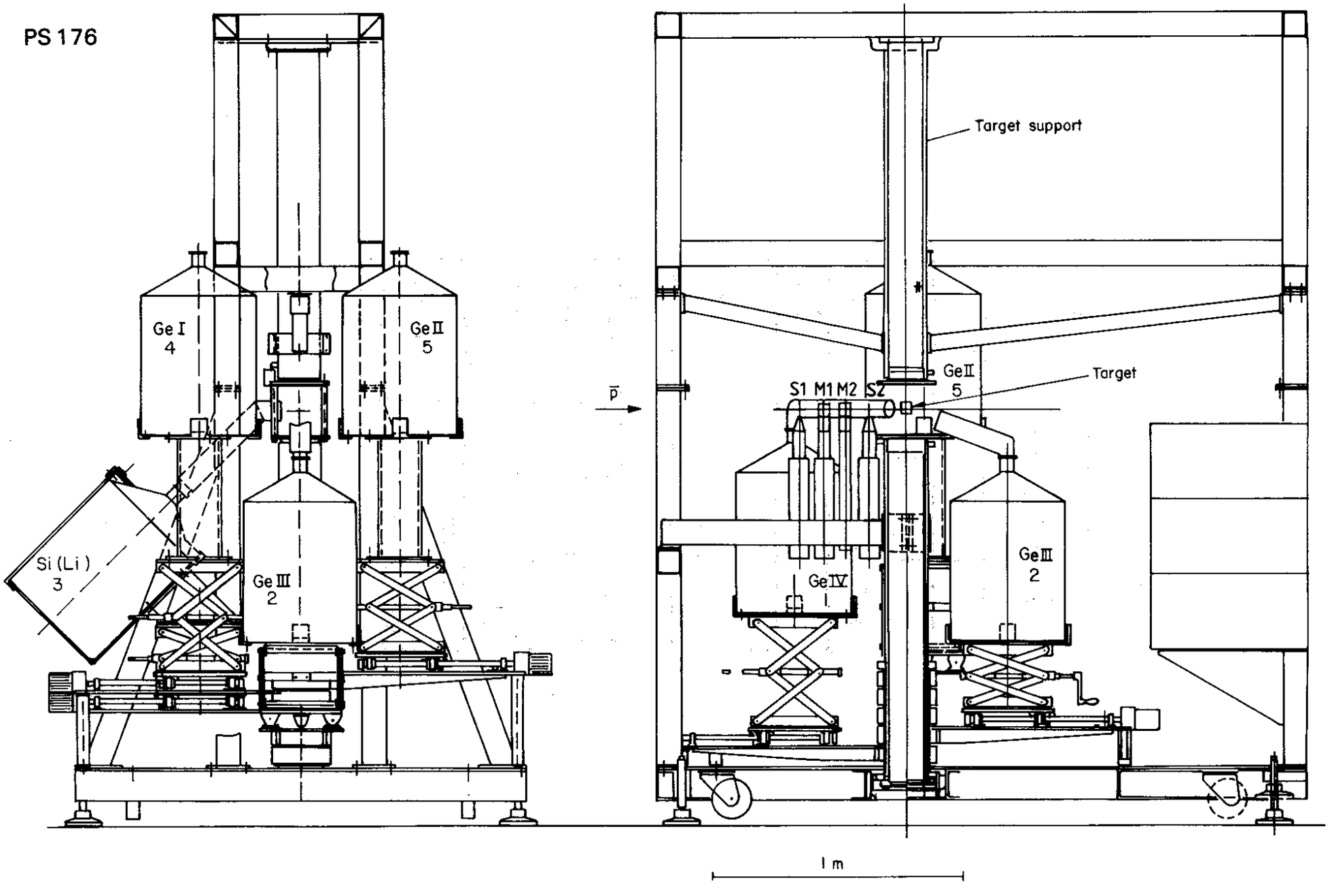
PS 176
Ge I
4
Ge II
5
Si (Li)
3
Ge III
2
p̄
Target support
S1 M1 M2 S2
Ge II
5
Target
Ge III
2
Ge IV
1
1 m

Fig. 1

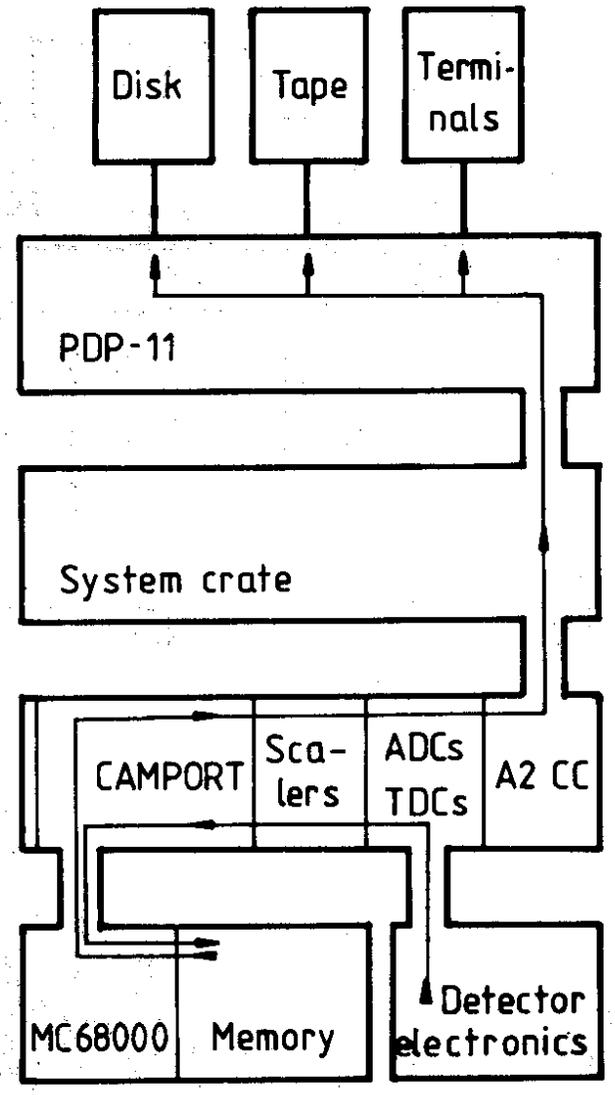
Disk
Tape
Termi-
nals
PDP-11
System crate
CAMPORT
Sca-
lers
ADCs
TDCs
A2 CC
MC68000
Memory
Detector
electronics

Fig. 2

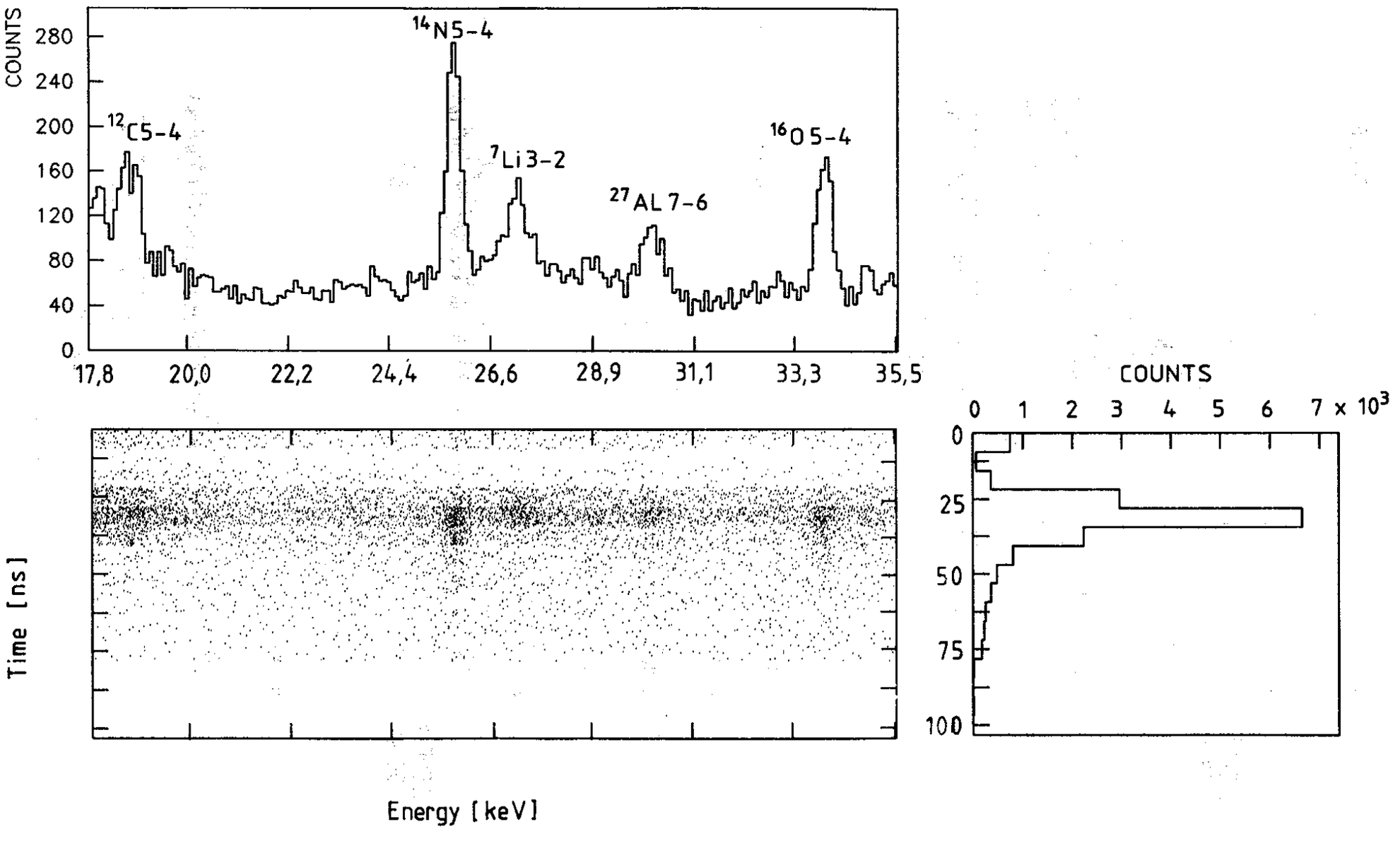
COUNTS
280
240
200
160
120
80
40
0
^{12}C5-4
^{14}N5-4
^{7}Li3-2
^{27}AL7-6
^{16}O5-4
17,8
20,0
22,2
24,4
26,6
28,9
31,1
33,3
35,5
Time [ns]
Energy [keV]
COUNTS
0 1 2 3 4 5 6 7 x 10^3
0
25
50
75
100

Fig. 3

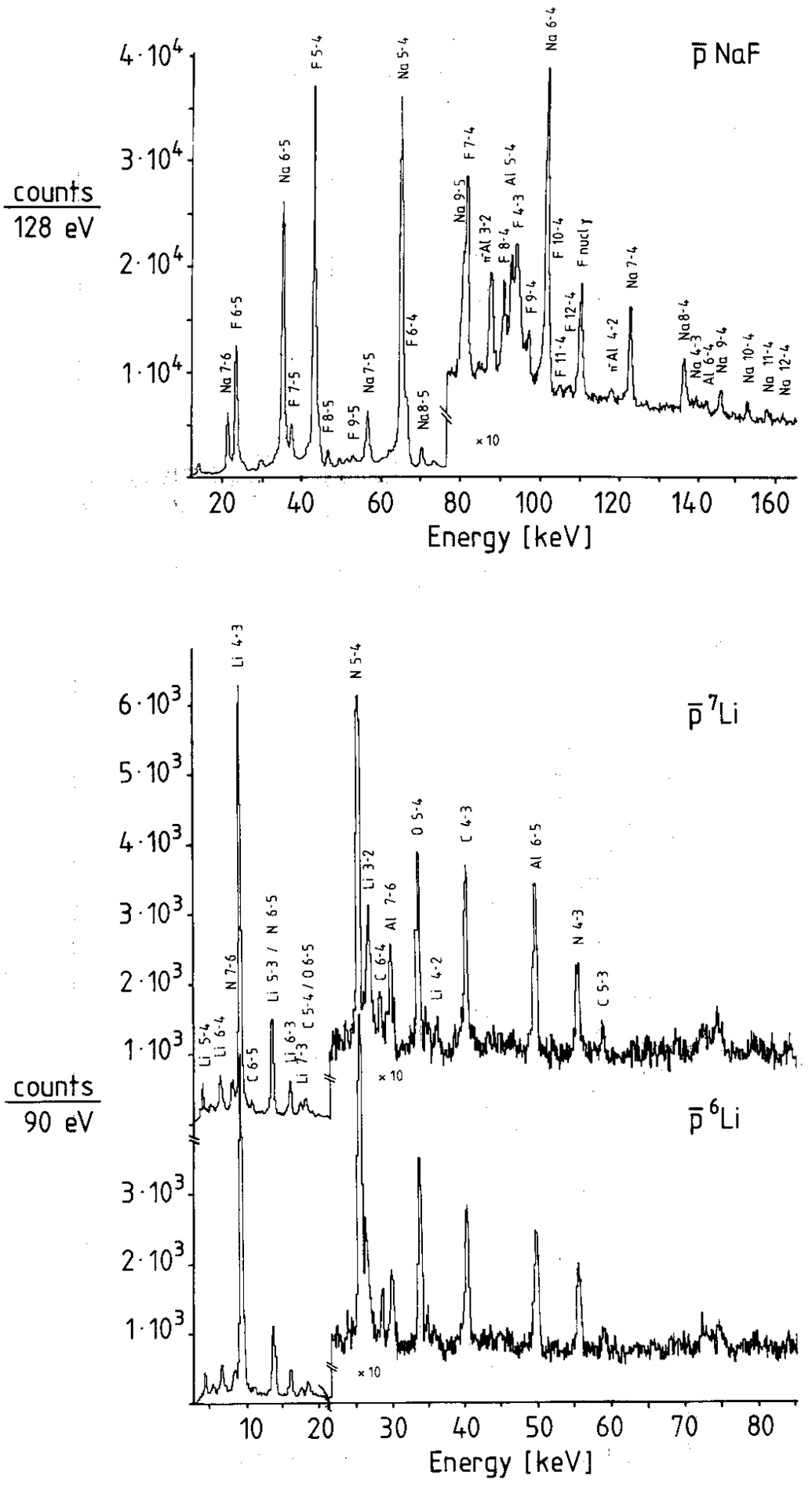
p̄ NaF
counts
128 eV
4·10^4
3·10^4
2·10^4
1·10^4
Na 7-6
F 6-5
Na 6-5
F 7-5
F 5-4
F 8-5
F 9-5
Na 7-5
Na 5-4
F 6-4
Na 8-5
Na 9-5
F 7-4
π Al 3-2
F 8-4
F 4-3
Al 5-4
F 9-4
Na 6-4
F 10-4
F 11-4
F 12-4
F nucl γ
π Al 4-2
Na 7-4
Na 8-4
Na 4-3
Al 6-4
Na 9-4
Na 10-4
Na 11-4
Na 12-4
× 10
20
40
60
80
100
120
140
160
Energy [keV]
p̄ 7Li
counts
90 eV
6·10^3
5·10^3
4·10^3
3·10^3
2·10^3
1·10^3
Li 5-4
Li 6-4
N 7-6
Li 4-3
C 6-5
Li 5-3 / N 6-5
Li 6-3
Li 7-3
C 5-4 / O 6-5
N 5-4
Li 3-2
Al 7-6
C 6-4
O 5-4
Li 4-2
C 4-3
Al 6-5
N 4-3
C 5-3
× 10
p̄ 6Li
3·10^3
2·10^3
1·10^3
× 10
10
20
30
40
50
60
70
80
Energy [keV]

Fig. 4

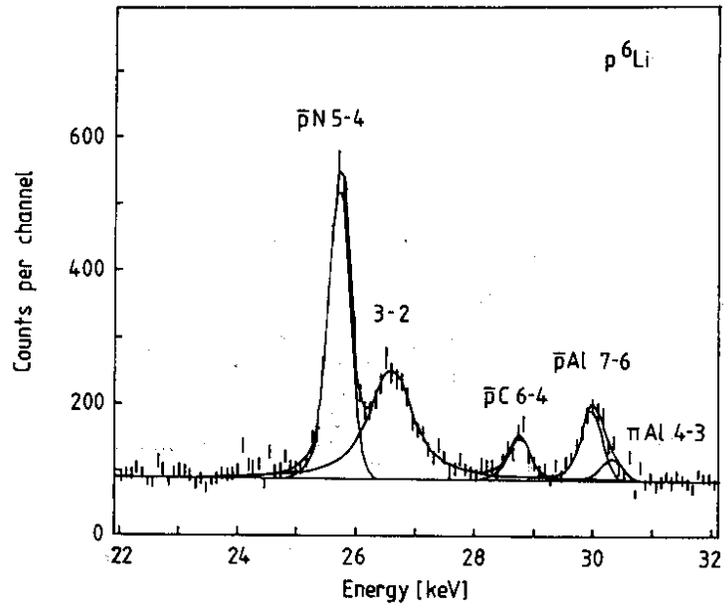
p 6Li
p̄N 5-4
3-2
p̄Al 7-6
p̄C 6-4
πAl 4-3
Counts per channel
Energy [keV]
0
200
400
600
22
24
26
28
30
32

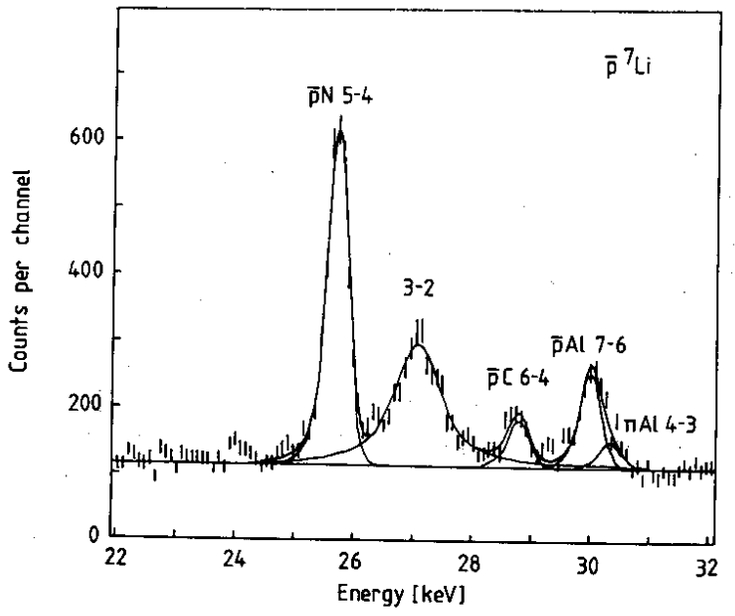
p̄ 7Li
p̄N 5-4
3-2
p̄Al 7-6
p̄C 6-4
πAl 4-3
Counts per channel
Energy [keV]
0
200
400
600
22
24
26
28
30
32

Fig. 5

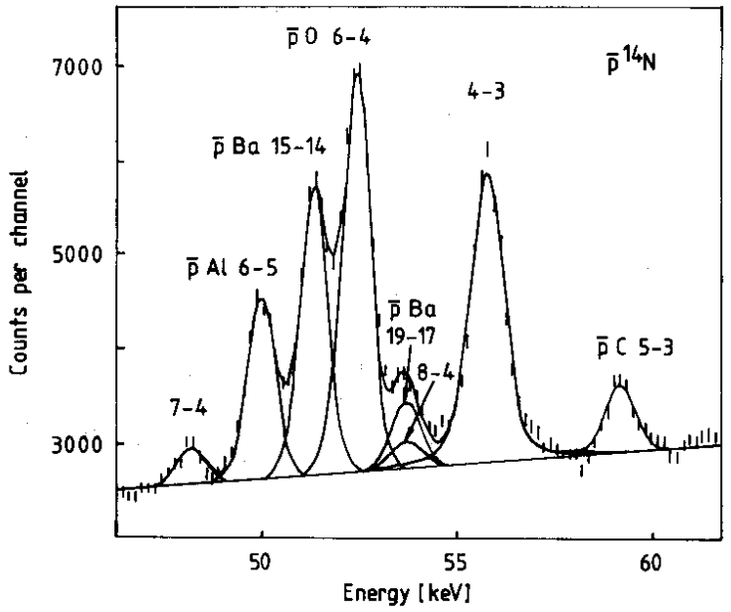
p̄ O 6-4
p̄ ^{14}N
4-3
p̄ Ba 15-14
p̄ Al 6-5
p̄ Ba 19-17
8-4
p̄ C 5-3
7-4
7000
5000
3000
Counts per channel
50
55
60
Energy [keV]

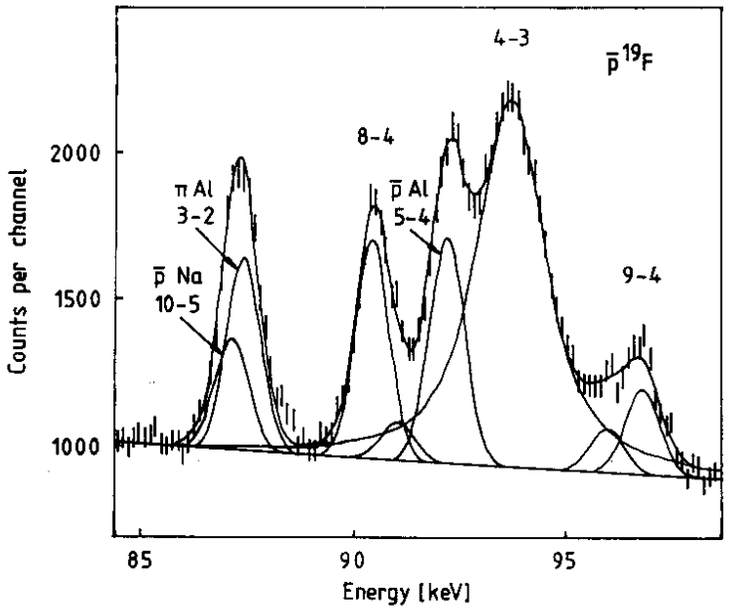
4-3
p̄ ^{19}F
8-4
π Al 3-2
p̄ Al 5-4
p̄ Na 10-5
9-4
2000
1500
1000
Counts per channel
85
90
95
Energy [keV]

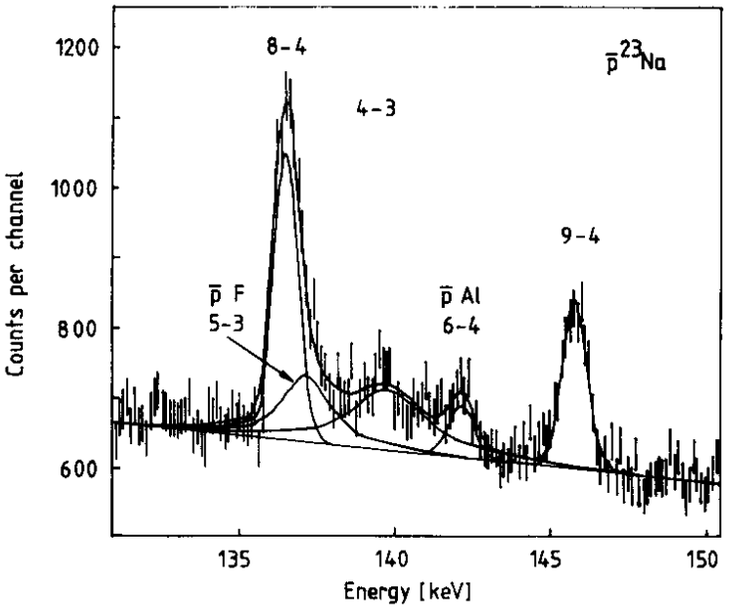
8-4
p̄ ^{23}Na
4-3
9-4
p̄ F 5-3
p̄ Al 6-4
1200
1000
800
600
Counts per channel
135
140
145
150
Energy [keV]

Fig. 6

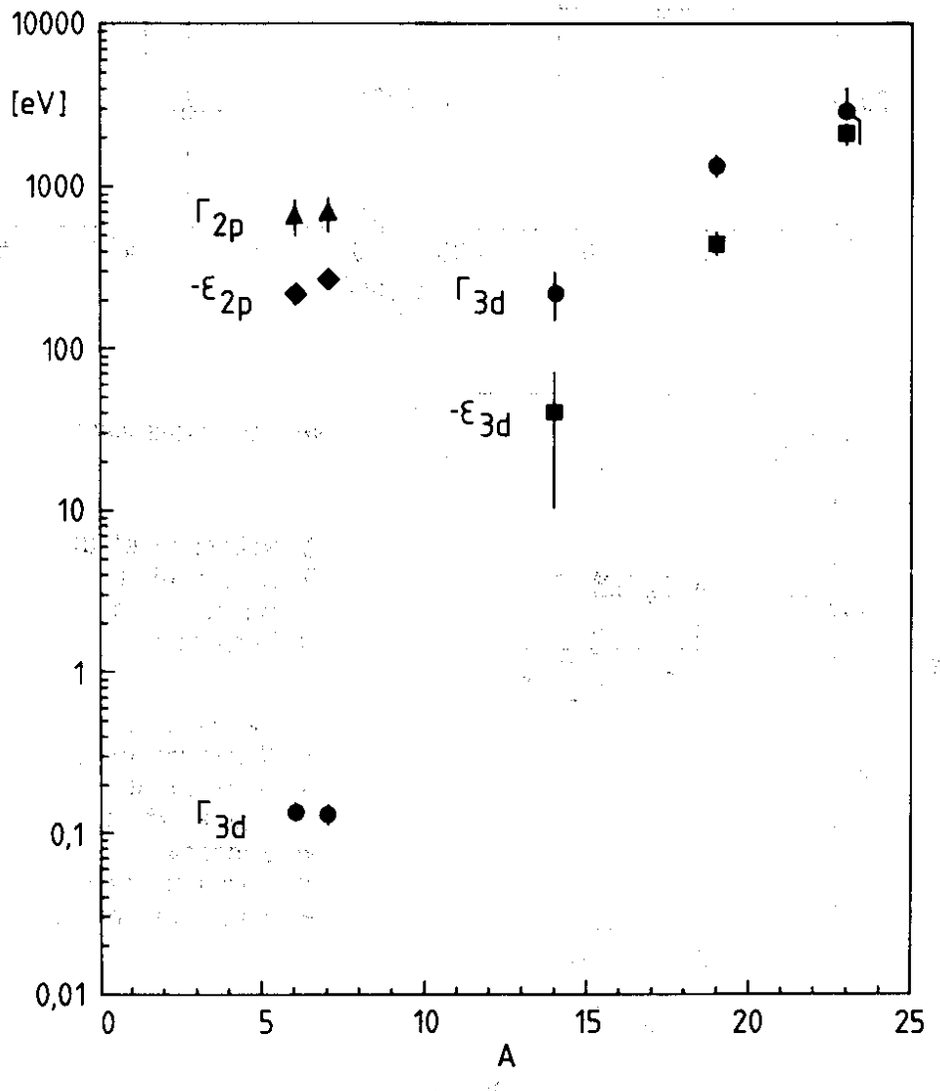

Fig. 7

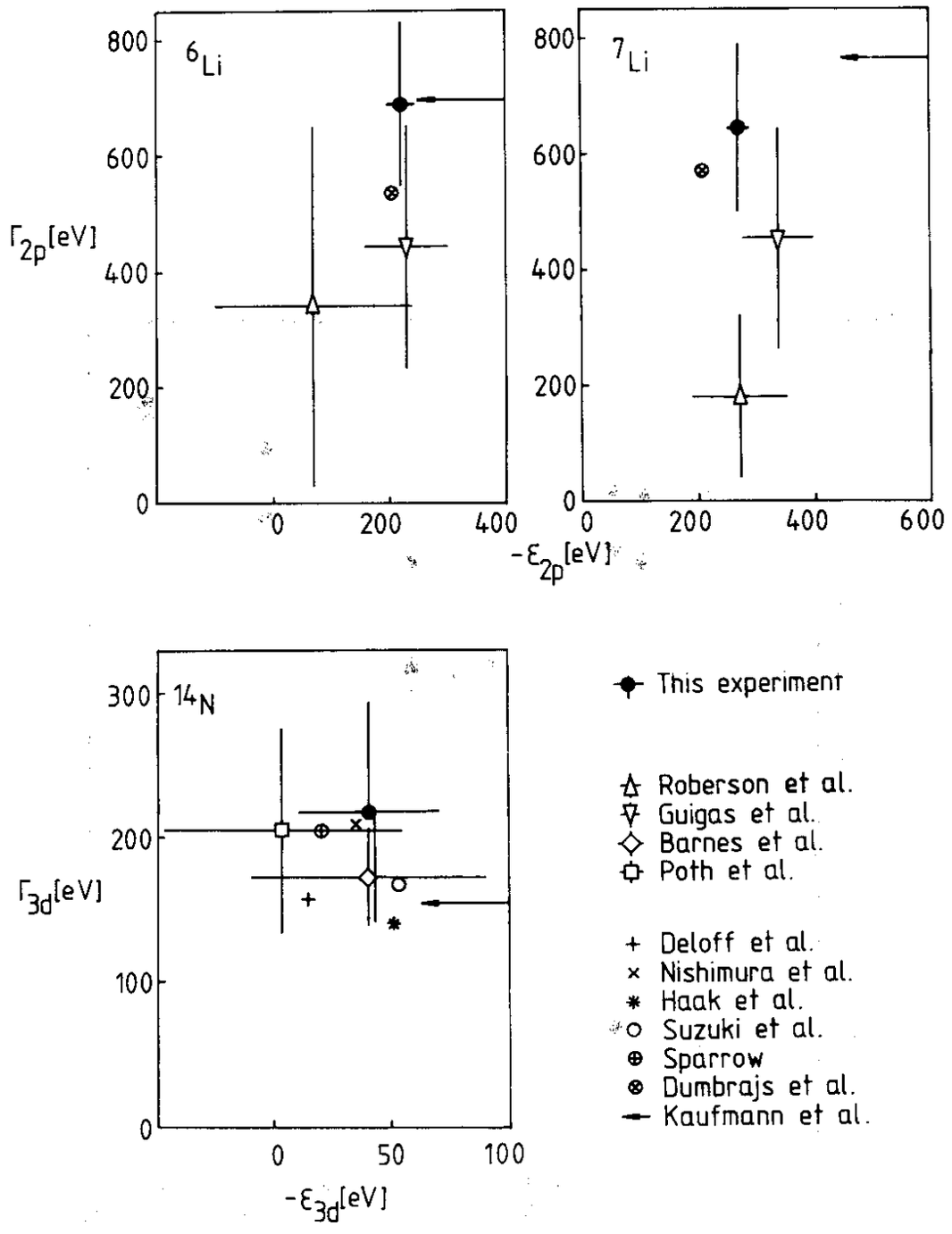
^{6}Li
^{7}Li
^{14}N
Γ_{2p}[eV]
$-\varepsilon_{2p}$[eV]
Γ_{3d}[eV]
$-\varepsilon_{3d}$[eV]
This experiment
Roberson et al.
Guigas et al.
Barnes et al.
Poth et al.
Deloff et al.
Nishimura et al.
Haak et al.
Suzuki et al.
Sparrow
Dumbrajs et al.
Kaufmann et al.

Fig. 8

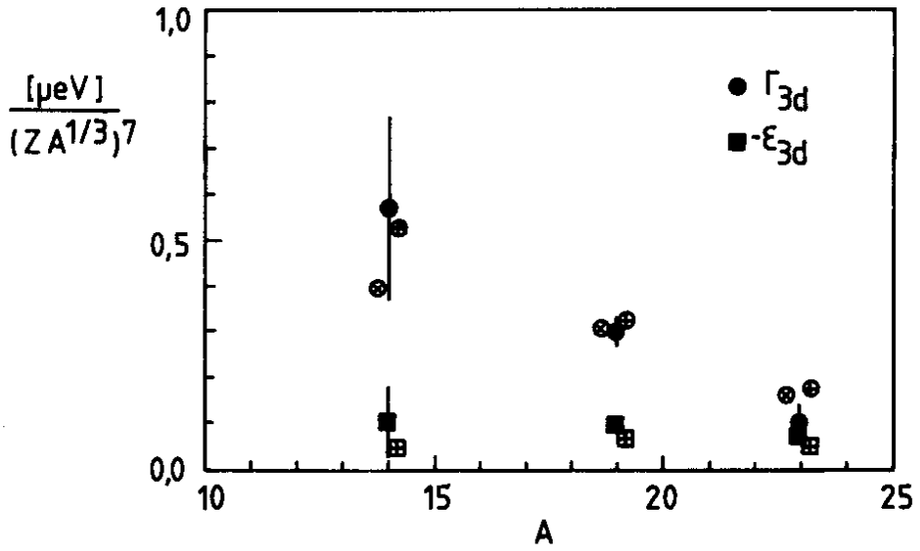

Fig. 9